hybrid model ages (Fig. 2A). However, using these data, and our relation that characterizes the proportion of new crust and hybrid model ages through time (Fig. 1B, Eqs. 1 and 2), we were able to calculate the distribution of new crust formation ages (Fig. 2A).

The net volume of new continental crust generated during magmatic episodes depends on the variations in the proportion of newly formed and reworked crust that is preserved through time. A broader proxy for the variations of the reworked crust through time is given by the distribution of the crystallization ages of zircons with Hf model ages greater than their crystallization ages (Fig. 2A). These variations may be linked to times of supercontinent assembly, periods that are characterized by both increased crustal reworking and preservational bias (8, 20, 21). The variation in the rates of crustal reworking through time, which is given by the variations in the proportions of the reworked crust versus calculated new crust, reveals low crustal reworking rates (< 20%) from the Hadean to the Meso-Archean. A rapid increase to around 75% reworking is observed at ~3 Ga, and then relatively high reworking rates (>50%) are observed until the present day.

This parameterization has several implications for models of the rates of growth of the continental crust (Fig. 2B). The distribution of Hf model ages, irrespective of their oxygen isotope ratios and the extent to which they include hybrid model ages (Fig. 2A), provides an estimate of the minimum volume of the preserved continental crust that was present through time, because it does not integrate the variations in the proportions of reworked and new crust. If, however, the model integrates crustal generation and reworking rates (Fig. 2A), we see that ~65% of the present-day volume of the crust was established by 3 Ga (Fig. 2B) and that there was a sharp change in the net rates of growth of the continental crust at that time. These features are not observed in continental growth curves calculated from large U-Pb and Hf in zircon databases in the absence of O isotope data (4).

Based on this analysis, we propose a two-stage model for continental growth (Fig. 2B). Stage 1 (>4 Ga to ~3 Ga) is characterized by relatively high net rates of continental growth. Given the present-day volume of the continental crust of 7.10^9 km^3 [e.g., (22)], the average net rate of growth of the continental crust for Stage 1 was ~3.0 km^3 year^{-1}. This is similar to the rates at which new crust is generated and destroyed at the present time (22, 23). The average net growth rate for Stage 2 (~3 Ga to the present day) is ~0.8 km^3 year^{-1}, and the inflection in the rate of crustal growth curve at ~3 Ga indicates a fundamental change in the way the continental crust was generated and preserved. The difference in the net rates of crustal growth in Stages 1 and 2 can be accommodated by high rates of destruction of continental crust in Stage 2 compared with Stage 1 (Fig. 2A). The inferred high crustal destruction rates in Stage 2 strongly

suggest that it reflects the onset of subduction-driven plate tectonics and discrete subduction zones at ~3 Ga, consistent with independent arguments from recent studies (24–26). Geodynamical processes that might have dominated in Stage 1 include shallow subduction and delamination (27) or "intraplate" lithospheric extension/mantle upwelling (26, 28), both of which could produce crust at rates similar to today (~3.0 km^3 year^{-1}).

References and Notes
1. K. C. Condie, *Earth Planet. Sci. Lett.* **163**, 97 (1998).
2. B. Dhuime, C. J. Hawkesworth, C. D. Storey, P. A. Cawood, *Geology* **39**, 407 (2011).
3. C. J. Allègre, D. Rousseau, *Earth Planet. Sci. Lett.* **67**, 19 (1984).
4. E. A. Belousova et al., *Lithos* **119**, 457 (2010).
5. C. J. Hawkesworth et al., *J. Geol. Soc. London* **167**, 229 (2010).
6. A. I. S. Kemp, C. J. Hawkesworth, B. A. Paterson, P. D. Kinny, *Nature* **439**, 580 (2006).
7. C. Y. Wang, I. H. Campbell, C. M. Allen, I. S. Williams, S. M. Eggins, *Geochim. Cosmochim. Acta* **73**, 712 (2009).
8. K. C. Condie, M. E. Bickford, R. C. Aster, E. Belousova, D. W. Scholl, *Geol. Soc. Am. Bull.* **123**, 951 (2011).
9. B. Dhuime, C. J. Hawkesworth, P. A. Cawood, *Science* **331**, 154 (2011).
10. D. J. DePaolo, *Nature* **291**, 193 (1981).
11. Materials and methods are available as supporting material on *Science* Online.
12. N. T. Arndt, S. L. Goldstein, *Geology* **15**, 893 (1987).
13. C. J. Hawkesworth, A. I. S. Kemp, *Chem. Geol.* **226**, 144 (2006).
14. J. W. Valley, P. D. Kinny, D. J. Schulze, M. J. Spicuzza, *Contrib. Mineral. Petrol.* **133**, 1 (1998).
15. J. W. Valley et al., *Contrib. Mineral. Petrol.* **150**, 561 (2005).
16. A. I. S. Kemp et al., *Science* **315**, 980 (2007).
17. A. B. Pietranik et al., *Geology* **36**, 875 (2008).
18. C. Y. Wang, I. H. Campbell, A. S. Stepanov, C. M. Allen, I. N. Burtsev, *Geochim. Cosmochim. Acta* **75**, 1308 (2011).
19. P. J. Voice, M. Kowalewski, K. A. Eriksson, *J. Geol.* **119**, 109 (2011).
20. I. H. Campbell, C. M. Allen, *Nat. Geosci.* **1**, 554 (2008).
21. C. J. Hawkesworth, P. A. Cawood, T. Kemp, C. Storey, B. Dhuime, *Science* **323**, 49 (2009).
22. D. W. Scholl, R. von Huene, in *Earth Accretionary Systems in Space and Time,* P. A. Cawood, A. Kröner, Eds. (Geological Society, London, Special Publications, 2009), vol. 318, pp. 105–125.
23. D. W. Scholl, R. von Huene, in *4-D Framework of Continental Crust,* R. D. Hatcher, M. P. Carlson, J. H. McBride, J. R. M. Catalán, Eds. (Geological Society of America Memoir, 2007), vol. 200, pp. 9–32.
24. P. A. Cawood, A. Kröner, S. Pisarevsky, *GSA Today* **16**, 4 (2006).
25. S. B. Shirey, S. H. Richardson, *Science* **333**, 434 (2011).
26. M. J. Van Kranendonk, *Science* **333**, 413 (2011).
27. S. F. Foley, S. Buhre, D. E. Jacob, *Nature* **421**, 249 (2003).
28. M. J. Van Kranendonk, *Am. J. Sci.* **310**, 1187 (2010).
29. P. J. Lancaster, C. D. Storey, C. J. Hawkesworth, B. Dhuime, *Earth Planet. Sci. Lett.* **305**, 405 (2011).
30. C. W. Rapela et al., *Gondwana Res.* **20**, 673 (2011).

The Multielectron Ionization Dynamics Underlying Attosecond Strong-Field Spectroscopies

Andrey E. Boguslavskiy,[1]* Jochen Mikosch,[1]* Arjan Gijsbertsen,[1,2]* Michael Spanner,[1] Serguei Patchkovskii,[1] Niklas Gador,[3] Marc J. J. Vrakking,[2,4] Albert Stolow[1]†

Subcycle strong-field ionization (SFI) underlies many emerging spectroscopic probes of atomic or molecular attosecond electronic dynamics. Extending methods such as attosecond high harmonic generation spectroscopy to complex polyatomic molecules requires an understanding of multielectronic excitations, already hinted at by theoretical modeling of experiments on atoms, diatomics, and triatomics. Here, we present a direct method which, independent of theory, experimentally probes the participation of multiple electronic continua in the SFI dynamics of polyatomic molecules. We use saturated (*n*-butane) and unsaturated (1,3-butadiene) linear hydrocarbons to show how subcycle SFI of polyatomics can be directly resolved into its distinct electronic-continuum channels by above-threshold ionization photoelectron spectroscopy. Our approach makes use of photoelectron-photofragment coincidences, suiting broad classes of polyatomic molecules.

To date, measurements of attosecond electronic dynamics in atoms and molecules (1) have typically involved strong laser-field processes. Even pump-probe spectroscopies using isolated attosecond pulses rely on the presence of a phased, strong (~10^{13} W/cm^2) laser field (2–4). The process of high harmonic gen-

eration (HHG), which can probe electronic wave packets on attosecond time scales (5–9), is entirely based on strong-field ionization (SFI), as is the use of subcycle electron recollision for probing dynamics (10, 11). In the interpretation of experiments, broad use is made of the three-step model (12) wherein SFI adiabatically releases, via

tunneling, a single continuum electron that is subsequently driven in the strong, oscillating laser field. However, even in simple diatomics, the possible role of multiple electronic continua in attosecond SFI measurements (5, 13, 14) is unclear (6, 15). In the complex world of multielectron polyatomic molecules, adiabatic single-electron tunneling approximations are very unlikely to hold (16–19). Nevertheless, to have broader impact, attosecond HHG spectroscopies must be extended to polyatomic molecules (20), and therefore, a general understanding of the role of multielectron SFI dynamics in polyatomics is required. Here, we introduce the channel-resolved above-threshold ionization (CRATI) method, where the channel refers to the electronic state of the ion correlated with the continuum electron. Independent of theoretical models, we experimentally resolve the multiple electronic continuum channels in SFI of polyatomic systems. By studying the CRATI of the linear hydrocarbons 1,3-butadiene and n-butane, we unambiguously demonstrate the direct, subcycle participation of multiple final ionic states in molecular SFI. We show that the population of higher-lying electronic continua can, depending on molecular properties, even exceed that of the ground state. We independently corroborate our experimental results with high-level, all-electron dynamical Schrödinger equation calculations. These combined results show that the relative contributions of these multiple continuum channels depend on both molecular electronic structure and laser-field properties and that both adiabatic and nonadiabatic laser-driven electronic dynamics may result.

A seminal attosecond transient absorption spectroscopy study recently demonstrated the coherent population (amplitudes and phases) of spin-orbit states due to SFI of krypton atoms (2). This technique benefitted from the presence of sharp features in the absorption spectrum that identified the two coherently prepared ionic states. To discern the ionic states of polyatomic molecules populated by SFI, alternate approaches might be required, because transient absorption spectroscopy of polyatomics is much more complex. Our experimental approach is based on above-threshold ionization (ATI) (21–24), a universal SFI phenomenon wherein a field-driven continuum electron absorbs excess photons beyond the minimum number required for ionization. This leads to observation of a series of peaks in the electron kinetic energy spectrum, spaced by the photon energy. There is a deep connection between ATI and the process of HHG. In

both cases, subcycle SFI generates a continuum electron that, depending on phase, either recollides with its ion core and emits a burst of extreme ultraviolet radiation (HHG) or accelerates away from the ion as an energetic electron (ATI). In either case, a single-cycle pulse would result in structureless HHG and ATI spectra. Structured spectra arise from this subcycle emission (photon or electron) being repeated every optical cycle. First evidence for the participation of multiple continua in HHG spectroscopy of molecules emerged from experiments on CO_2 (5, 25), N_2 (6, 26, 27), and N_2O_4 (28), each relying strongly on theoretical modeling for interpretation. These results caution that essential multiple continuum effects should not be ignored. Such effects are to be expected in the SFI of polyatomic molecules, because their many valence electrons should all respond to the strong laser electric field. We find, for the molecules studied here, that electrons can be ejected by tunneling via independent channels, populating the ionic ground state [ejection of the highest occupied molecular orbital (HOMO) electron;

i.e., HOMO ionization] and/or excited (for instance, HOMO–1 ionization) electronic states. By independent, we mean that the continuum channels remain uncoupled (that is, no transitions between them) in the laser field. However, in other molecular systems and/or at higher laser intensity, nonadiabatic interchannel coupling can occur during SFI. In this situation, another bound electron makes a laser-induced transition on a subcycle time scale as the continuum electron departs. This process is termed nonadiabatic multielectron (NME) ionization (16) and will be discussed below. Whether the response is adiabatic or not, population of multiple electronic continua will be a generic feature of SFI of polyatomic molecules. To distinguish SFI channels populating the ionic ground-state continuum from those populating ionic excited-state continua, we make use of the fact that, unlike diatomics, electronically excited polyatomic ions generally undergo rapid radiationless transitions, which leads to fragmentation (29, 30). This is the case for the linear hydrocarbons studied here, 1,3-butadiene (C_4H_6) and n-butane (C_4H_{10}):

Table 1. Vertical field-free ionization potentials I_P^{FF} and Stark-shifted ionization potentials I_P^{SS} (in electron volts) of the first four ionic states $(D_j, j = 0$ to 3) of n-butane and three ionic states $(D_j, j = 0, 1, 2)$ of 1,3-butadiene. The I_P^{FF} are measured values taken from (38) unless otherwise indicated. I_P^{SS} values include the calculated Stark shift of the jth ionization potential, as described in the SOM. As the CRATI measurements were performed in presence of the laser field, the I_P^{SS} values pertain for comparison with experiment.

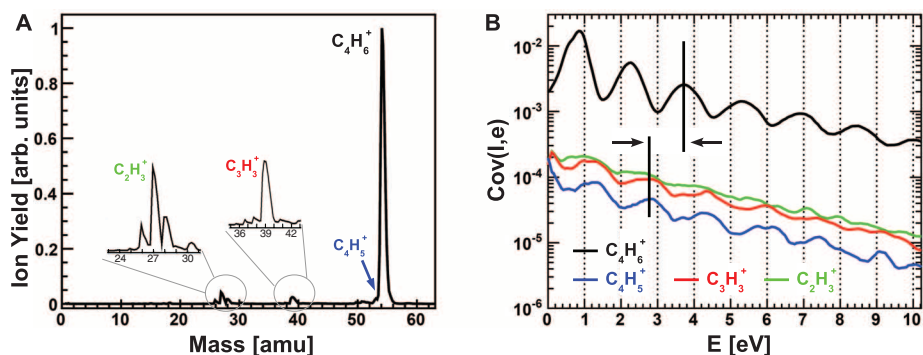| Ionic state	Ionization potential	n-Butane	1,3-Butadiene
D_0	I_P^{FF}	11.2	9.29*
	I_P^{SS}	11.0	9.2
D_1	I_P^{FF}	11.7	11.48*
	I_P^{SS}	11.4	11.5
D_2	I_P^{FF}	11.7	12.2
	I_P^{SS}	11.5	11.7
D_3	I_P^{FF}	12.2	(Not used)
	I_P^{SS}	12.2	

*Taken from (39)

Fig. 1. Strong-field ionization of 1,3-butadiene at a peak intensity of 1.9×10^{13} W/cm². (**A**) Mass spectrum with the most prominent peak being the parent $C_4H_6^+$ ion. Fragment ions $C_4H_5^+$, $C_3H_3^+$, and $C_2H_3^+$ that originate from the unstable D_1 excited ion state were also observed. amu, atomic mass units. (**B**) CRATI photoelectron spectra correlated with both parent and fragment ions. As indicated by the vertical lines, the fragment CRATI combs are shifted in energy relative to that of the parent ion (black) by 0.95 ± 0.05 eV. This is quantitatively the energy difference between the Stark-shifted D_0 and D_1 ionic states in 1,3-butadiene, modulo the photon energy, which unambiguously demonstrates that the excited D_1 ion state was directly populated from the neutral ground state. For a detailed discussion, see the text.

[1]Steacie Institute for Molecular Sciences, National Research Council of Canada, Ottawa, Ontario K1A 0R6, Canada. [2]FOM Instituut voor Atoom-en Molecuulfysica (AMOLF), Science Park 102, 1098 XG Amsterdam, Netherlands. [3]Department of Chemical Physics, Lund University, Box 124, SE-22100 Lund, Sweden. [4]Max-Born-Institute, Max Born Strasse 2A, D12489, Berlin, Germany.

*These authors contributed equally to this work.
†To whom correspondence should be addressed. E-mail: albert.stolow@nrc.ca

Only their ionic electronic ground state is stable, whereas transitions to electronically excited ionic states lead to unimolecular dissociation of the parent ion, producing fragments on a time scale much longer than the laser interaction (*31–33*). However, in a strong laser field, fragment ions may also be produced by postionization excitation of the ionic ground state. Therefore, the observation of ionic fragmentation in itself does not constitute proof that the SFI process directly populates electronically excited ionic states. Experimentally, we need to distinguish two SFI pathways: (i) subcycle ionization directly into an ionic excited state versus (ii) ionization forming the ionic ground state, followed by subsequent excitation during the laser cycles after ionization. In our CRATI experiment, this is achieved by measuring the ATI kinetic energy spectrum in coincidence (or covariance) with parent and fragment ions. As described in the supporting online material (SOM), the covariance-mapping method reveals correlations between ions and electrons via statistical analysis of count-rate fluctuations (*34*). The ATI spectrum consists of a comb of electron kinetic energies spaced by the photon energy (Eq. 1)

$$E = m\hbar\omega - [I_P^{(D_j)} - U_P] \qquad (1)$$

where m is an integer and $\hbar\omega$ is the photon energy. For the molecular core, $I_P^{(D_j)}$ is the Stark-shifted molecular ionization potential of the jth ionization channel (where $j = 0$ signifies the D_0 ground electronic state of the ion, $j = 1$ the D_1 first excited electronic state of the ion, and so forth) and accounts for the relative Stark shifts of both neutral and ionic states. U_P is the ponderomotive (quiver) energy of a free electron (charge e, mass m_e) in an oscillating laser field of angular frequency ω and electric field amplitude E_0 (Eq. 2)

$$U_P = \frac{e^2 E_0^2}{4 m_e \omega^2} \qquad (2)$$

As described in detail in the SOM, the Stark-shifted ionization potential $I_P^{(D_j)}$ is the field-free ionization potential plus the difference in Stark shift between the neutral ground state and the jth ionization channel. Due to their differing $I_P^{(D_j)}$, the different ionization channels will have ATI combs shifted with respect to each other. If direct SFI to an electronically excited ion state D_j occurs, the correlated ion fragments will exhibit an ATI comb shifted relative to that correlated with the parent ion. In contrast, if ion excited states were populated subsequently by postionization excitation, meaning that the continuum electron has departed before further excitation occurs, then the fragments would have the same ATI spectrum as the parent ion because postionization excitation can no longer influence the departed continuum electron. Note that whereas several electronically excited ionization channels might correlate with the same ion fragment,

the parent ion will uniquely identify the D_0 ground-state ionization channel. By our method, we can determine whether SFI directly produced ionic ground or excited states, or whether ionic excited states were sequentially populated after removal of the electron. In Table 1 and table S1, we list the vertical and Stark-shifted ionization potentials $I_P^{(D_j)}$ of the lowest four ionic electronic states for the molecules studied here. As seen from Eqs. 1 and 2, the ATI shift depends on laser intensity and, therefore, spatial averaging over the laser focal volume reduces the contrast of the ATI peaks. As discussed in the SOM, we explicitly minimized this effect by using a restricted target volume geometry. We obtained absolute intensity calibrations by studying the shift of the ATI combs with laser intensity (i.e., U_P) for the H_2O molecule, in which the molecular Stark shifts are negligible. In our measurements, the value of U_P in Eq. 1 is very similar for all participating ionic states. This is because, for the low count-rate requirements of our covariance experiment, ionization is spatially restricted to the very center of the laser focus. In SFI, possible excited-state resonances in the neutral molecule can produce the well-known Freeman resonances (*35*), leading to sharp features in the ATI spectra, which have a limited progression. We indeed observed Freeman resonances in these molecular systems (see fig. S2 and accompanying text), as confirmed by their laser-intensity independence. In contrast, the ATI peaks shift monotonically with laser intensity. In low-frequency fields, the Freeman resonances contribute only to the first two or three ATI peaks: The shifts reported here are based on the higher members of the ATI progression. Therefore, the possible excitation of neutral excited states does not affect our analysis of the ATI comb shifts. By studying CRATI as a function of the ellipticity of the driving field, we furthermore confirmed that electron recollision played no important role in producing excited states.

The details of the experimental geometry, data collection, and analysis are presented in the SOM. In Fig. 1, we present the mass spectrum

(left) and normalized CRATI photoelectron spectra (right) for 1,3-butadiene at a peak intensity of 1.9×10^{13} W/cm^2 ($\hbar\omega = 798$ nm/1.55 eV, $U_P = 1.16$ eV). The mass spectrum is strongly dominated by the parent ion $C_4H_6^+$, which accounts for 87% of the overall ion yield. This number directly gives a lower limit for the probability of formation of the D_0 ionic ground electronic state in SFI of 1,3-butadiene, corresponding to HOMO ionization. A small (13%) contribution from fragments is also seen in the mass spectrum, indicating population of ionic excited states. As a percent ratio of the parent ion signal, the most prominent fragmentation channels are $C_4H_5^+$ (1%), $C_3H_3^+$ (3%), and $C_2H_3^+$ (3%). The CRATI photoelectron spectra (right) show a series of peaks spaced by the photon energy, as expected. The CRATI peaks correlated with the parent $C_4H_6^+$ ion yield a comb associated with ionization into the $X(D_0)$ ground state. In Fig. 1B, the vertical lines indicate the relative shift of the ATI combs, determined from analysis of the higher-order peaks contributing to each comb. Relative to the $C_4H_6^+$ comb, the CRATI combs of the $C_4H_5^+$ and $C_3H_3^+$ fragment channels are both shifted toward lower energy by 0.95 ± 0.05 eV, as determined by statistical analysis of the relative comb shifts. This is unambiguous experimental evidence of direct SFI into ion excited states in 1,3-butadiene: Postionization fragmentation of the D_0 ground state could not produce this result. From Table 1, the Stark-shifted $D_1(^2A_u)$ and $D_2(^2A_g)$ states of the 1,3-butadiene ion lie 2.3 and 2.5 eV above the Stark-shifted $D_0(^2B_g)$ ground state, respectively. The ATI comb shift can only be observed modulo the photon energy (1.55 eV). Therefore, direct SFI to the $D_1(^2A_u)$/$D_2(^2A_g)$ states should produce an average CRATI comb shifted relative to that of the ground state by 2.40 − 1.55 = 0.85 eV. Within errors, this is quantitatively the shift observed for the $C_4H_5^+$ and $C_3H_3^+$ CRATI combs. This conclusion is further supported by prior tunable vacuum ultraviolet single-photon ionization studies on 1,3-butadiene, which showed that the $C_4H_5^+$ and $C_3H_3^+$ fragments appear as soon as the $D_1(^2A_u)$ ion state
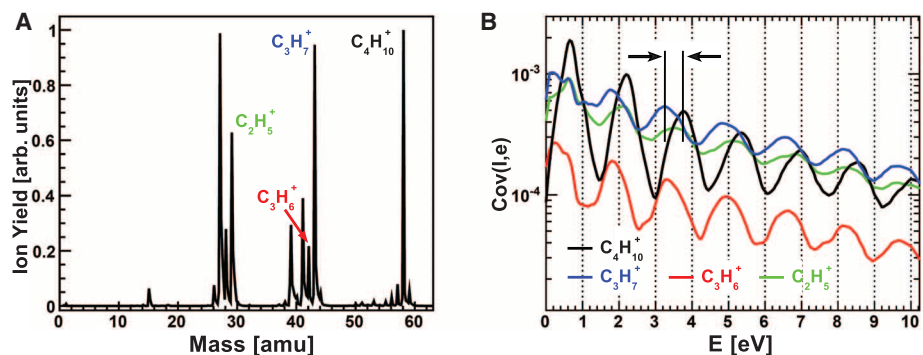

Fig. 2. Strong-field ionization of *n*-butane at a peak intensity of 1.6×10^{13} W/cm^2. (**A**) Mass spectrum. (**B**) CRATI photoelectron spectra correlated with different fragment ions. Extensive fragmentation occurs even at low intensity. Several fragment CRATI combs show a shift relative to that of the parent ion (black). These can be quantitatively assigned to originate from direct SFI into excited ionic states.

is energetically accessible (32). In contrast, the $C_2H_3^+$ fragment has an appearance energy more than 6 eV above that of the parent ion (32). In our experiment, $C_2H_3^+$ probably originates from further excitation of the ion in subsequent field cycles. As can be seen in Fig. 1B, the $C_2H_3^+$ CRATI spectrum exhibits fairly washed out ATI structure with little modulation depth, consistent with several SFI channels contributing to the formation of this fragment. We can rule out the population of neutral excited states within the laser pulse, leading to their SFI and associated ATI comb: This is not consistent with the present results because the lower I_P (which determines their ATI comb shift) of a neutral excited state does not match those due to ionization of the neutral ground state.

In Fig. 2, we present mass (left) and CRATI spectra (right) for n-butane at a peak intensity of 1.6×10^{13} W/cm^2 ($\hbar\omega = 798$ nm/1.55 eV, $U_P = 0.93$ eV). In contrast to 1,3-butadiene, n-butane predominantly fragments upon ionization, producing $C_3H_n^+$ and $C_2H_n^+$ ions. The $C_3H_7^+$ and $C_3H_6^+$ fragments are associated with populating the first ionic excited state, whereas the $C_2H_5^+$ fragment is known to be associated with the third ionic excited state (33). Relative to the parent ion signal, the percent ratio of the fragment ions are: $C_3H_7^+$ (122%), $C_3H_6^+$ (27%), $C_2H_5^+$ (96%), and $C_2H_3^+$ (152%). Figure 2B shows that the $C_3H_7^+$ fragment CRATI comb (blue) is shifted to lower energy by 0.45 ± 0.05 eV relative to the parent ion comb (black). As seen in Table 1, the energy difference between the Stark-shifted D_0 ion ground state and the field-split $D_1(^2B_g)/D_2(^2A_g)$ ionic excited states of n-butane is 0.4/0.5 eV, in

quantitative agreement with the shift of the $C_3H_7^+$ comb (blue) in Fig. 2B. This reveals that the dominant $C_3H_7^+$ channel is due to direct SFI into the first excited ionic state. Figure 2B also shows that the $C_3H_6^+$ CRATI comb (red) is shifted to lower energy by 0.40 ± 0.05 eV relative to the parent ion comb. Therefore, within experimental error, we can also associate $C_3H_6^+$ with direct SFI into the first ion excited state. The $C_2H_5^+$ (green) and $C_2H_3^+$ (see SOM) fragment combs are both shifted to lower energy by 0.10 ± 0.05 eV relative to the parent ion comb. Although this shift is not in strict quantitative agreement with the data given in Table 1, within the approximations used in calculating the excited-state polarizabilities, it is consistent with direct SFI into the third ion excited state. The CRATI results for n-butane show that SFI to electronically excited continuum channels can dominate over SFI to the ground state. In sum, the combined results of Figs. 1 and 2 experimentally demonstrate that multiple continua do participate in the direct SFI of polyatomic molecules, with the relative contributions of these channels depending on molecular electronic structure. In the following, we interpret these observations in terms of the attosecond molecular SFI response.

The experimental results are independently (that is, using no adjustable parameters) corroborated by all-electron, coupled-channel time-dependent Schrödinger equation (TDSE) calculations, which are outlined in detail in the SOM. Briefly, this mixed orbital/grid-based approach (36) makes no assumptions about the nature of the ionization mechanism or the adiabaticity of the field-driven electron response. The neutral ground state

and the ground and excited ionic states are treated at an appropriate level of ab initio electronic structure theory. Both the bound electrons and the continuum electron are treated in the full three spatial dimensions, whereas the nuclei are kept frozen at the ground-state neutral geometry. The only central approximations are that: (i) a finite number of final ion electronic states are included (seven for 1,3-butadiene, eight for n-butane), and (ii) upon excitation, the departing electron is no longer antisymmetrized with respect to the remaining ionic core electrons. Our method supports multiple electronic excitations within the neutral molecule. We calculated the channel-resolved ionization yields to each of the ionic electronic states. To compare with experiment, we additionally averaged these channel-resolved ionization rates over the random lab frame distribution of molecules axes. We calculated the ionization rates using a single half-cycle of the driving laser field, reflecting the subcycle ionization rates and excluding any multicycle response. The use of a half-cycle pulse is discussed and justified in the SOM. In Fig. 3A, we present the results of the calculated channel-resolved SFI yields for the dominant conformers (insets) of 1,3-butadiene (left) and n-butane (right) at a peak intensity of 1.5×10^{13} W/cm^2. For 1,3-butadiene, ionization into the ionic ground state is the dominant channel, with some direct ionization into the first electronically excited state and higher lying channels. This result is in good agreement with the mass spectrum and CRATI results shown in Fig. 1. For the dominant anticonformer of n-butane (right), the calculations show that SFI into the first and higher lying electronically excited ionic
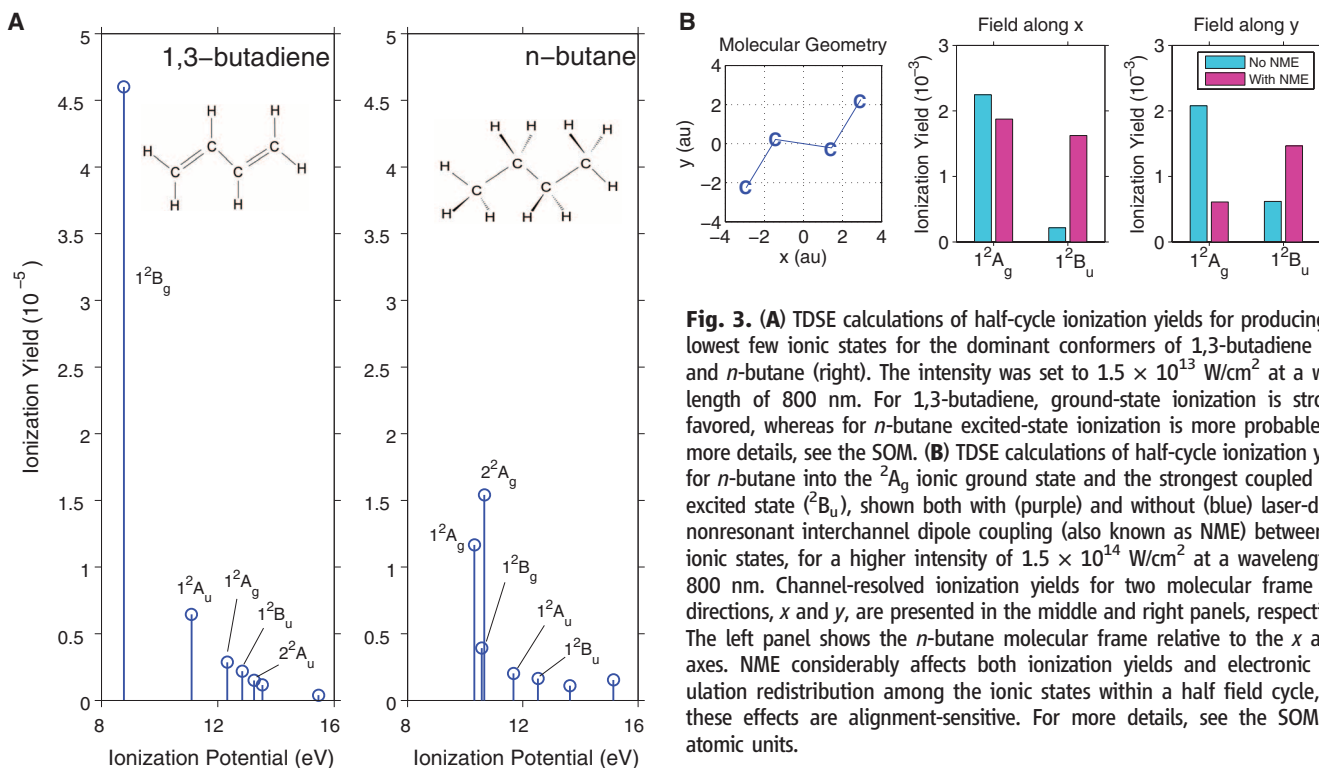

Fig. 3. (A) TDSE calculations of half-cycle ionization yields for producing the lowest few ionic states for the dominant conformers of 1,3-butadiene (left) and n-butane (right). The intensity was set to 1.5×10^{13} W/cm^2 at a wavelength of 800 nm. For 1,3-butadiene, ground-state ionization is strongly favored, whereas for n-butane excited-state ionization is more probable. For more details, see the SOM. **(B)** TDSE calculations of half-cycle ionization yields for n-butane into the ^2A_g ionic ground state and the strongest coupled ionic excited state (^2B_u), shown both with (purple) and without (blue) laser-driven nonresonant interchannel dipole coupling (also known as NME) between the ionic states, for a higher intensity of 1.5×10^{14} W/cm^2 at a wavelength of 800 nm. Channel-resolved ionization yields for two molecular frame field directions, x and y, are presented in the middle and right panels, respectively. The left panel shows the n-butane molecular frame relative to the x and y axes. NME considerably affects both ionization yields and electronic population redistribution among the ionic states within a half field cycle, and these effects are alignment-sensitive. For more details, see the SOM. au, atomic units.

states is favored over the ground-state channel. Once again, this agrees well with the experimental mass spectrum and CRATI results for *n*-butane (Fig. 2). These theoretical results show that direct ionization into multiple ionic states can be understood as a subcycle phenomenon. Qualitatively, the SFI response of these two molecules can be understood by considering the ionization energies and Dyson orbitals given in table S4. The Dyson orbitals represent the initial single-particle state of the ionizing electron. Within the Hartree-Fock approximation and Koopmans picture, they become ionization channels from the HOMO, HOMO–1, HOMO–2, etc. In a tunneling picture, SFI depends exponentially on the I_P through the Keldysh factor $\exp[-(2/3)(2I_P)^{3/2}/E_0]$. Furthermore, for diatomics (*37*) it is known that nodal planes in the Dyson orbitals can cause strong suppression of the total yield of SFI. For the case of 1,3-butadiene, although the 1^2A_u excited state has fewer nodal planes than the 1^2B_g ground state, the large energy gap favors the ground state. For the case of *n*-butane, where the energy gaps are much smaller, orbital symmetry effects become more pronounced. The Dyson orbitals for *n*-butane reveal that the 2^2A_g excited state has the fewest nodal planes; hence, this state experiences the least suppression, rendering it the dominant SFI channel as seen in Fig. 3A.

An important question is the role of laser-driven nonadiabatic interchannel coupling (also known as NME) in polyatomics. As discussed in the SOM, the hydrocarbons irradiated here at a peak intensity of ~10^{13} W/cm^2 (798 nm) exhibited predominantly adiabatic multichannel SFI dynamics. However, at higher intensities, the role of NME in even simple diatomics remains under active debate (*6*, *15*). With our TDSE method, we can artificially turn off the laser-driven interchannel coupling in the theory and compare the result to the case where the coupling is retained. This procedure accentuates the effects of NME on the ionic-state population distribution during SFI. In Fig. 3B, we present theoretical channel-resolved SFI yields in *n*-butane using a half-cycle pulse of higher intensity (1.5×10^{14} W/cm^2, 800 nm), both with (purple) and without (blue) NME coupling. For simplicity, only the ^2A_g ground state and the ^2B_u excited state were included, as these are the continuum channels most strongly dipole-coupled by the field. As seen in Fig. 3B, along two molecular frame directions *x* (middle) and *y* (right), coherent subcycle redistribution of population between electronic continuum channels occurs when NME is included. This qualitatively demonstrates that, at intensities typical of HHG experiments, the nonadiabatic population of multiple electronic continua can be another important contributor to the attosecond molecular response.

Although the present study does not address the tacit coherences created between ionic states (*2*), the CRATI method directly reveals the population of multiple electronic continua

in the SFI of polyatomic molecules. A future extension of this method that measures fragment ion energy and/or angular distributions will be of interest. Studying CRATI spectra as a function of molecular electronic structure, molecular frame alignment, and laser frequency/intensity will illuminate the role of multiple electronic continua in attosecond SFI spectroscopies such as HHG.

References and Notes

1. F. Krausz, M. Yu. Ivanov, *Rev. Mod. Phys.* **81**, 163 (2009).
2. E. Goulielmakis *et al.*, *Nature* **466**, 739 (2010).
3. G. Sansone *et al.*, *Nature* **465**, 763 (2010).
4. M. Uiberacker *et al.*, *Nature* **446**, 627 (2007).
5. O. Smirnova *et al.*, *Nature* **460**, 972 (2009).
6. S. Haessler *et al.*, *Nat. Phys.* **6**, 200 (2010).
7. H. J. Wörner, J. B. Bertrand, D. V. Kartashov, P. B. Corkum, D. M. Villeneuve, *Nature* **466**, 604 (2010).
8. J. Itatani *et al.*, *Nature* **432**, 867 (2004).
9. C. Vozzi *et al.*, *Appl. Phys. Lett.* **97**, 241103 (2010).
10. Y. Huismans *et al.*, *Science* **331**, 61 (2011).
11. M. Meckel *et al.*, *Science* **320**, 1478 (2008).
12. P. B. Corkum, *Phys. Rev. Lett.* **71**, 1994 (1993).
13. X.-B. Zhou *et al.*, *Phys. Rev. Lett.* **102**, 073902 (2009).
14. H. Akagi *et al.*, *Science* **325**, 1364 (2009).
15. S. Petretti, Y. V. Vanne, A. Saenz, A. Castro, P. Decleva, *Phys. Rev. Lett.* **104**, 223001 (2010).
16. M. Lezius *et al.*, *Phys. Rev. Lett.* **86**, 51 (2001).
17. M. Smits, C. A. de Lange, A. Stolow, D. M. Rayner, *Phys. Rev. Lett.* **93**, 203402 (2004).
18. A. N. Markevitch *et al.*, *Phys. Rev. A* **68**, 011402 (2003).
19. Z. B. Walters, S. Tonzani, C. H. Greene, *J. Phys. Chem. A* **112**, 9439 (2008).
20. D. J. Fraser *et al.*, *J. Phys. B* **28**, L739 (1995).
21. P. Agostini, F. Fabre, G. Mainfray, G. Petite, N. Rahman, *Phys. Rev. Lett.* **42**, 1127 (1979).
22. K. J. Schafer, B. Yang, L. F. DiMauro, K. C. Kulander, *Phys. Rev. Lett.* **70**, 1599 (1993).
23. C. I. Blaga *et al.*, *Nat. Phys.* **5**, 335 (2009).
24. H. Rottke, J. Ludwig, W. Sandner, *J. Phys. At. Mol. Opt. Phys.* **29**, 1479 (1996).
25. X. Zhou *et al.*, *Phys. Rev. Lett.* **100**, 073902 (2008).
26. B. K. McFarland, J. P. Farrell, P. H. Bucksbaum, M. Gühr, *Science* **322**, 1232 (2008).
27. I. Thomann *et al.*, *J. Phys. Chem. A* **112**, 9382 (2008).
28. W. Li *et al.*, *Science* **322**, 1207 (2008).
29. P. B. Armentrout, T. Baer, *J. Phys. Chem.* **100**, 12866 (1996).
30. W. A. Chupka, in *Chemical Spectroscopy and Photochemistry in the VUV*, C. Sandorfy, P. Ausloos, M. B. Robin, Eds. (North Atlantic Treaty Organization Advanced Study Institute Series, Reidel, Dordrecht, 1974), pp. 433–464.
31. R. Bombach, J. Dannacher, J.-P. Stadelmann, *J. Am. Chem. Soc.* **105**, 1824 (1983).
32. J. Dannacher, J.-P. Flamme, J.-P. Stadelmann, J. Vogt, *Chem. Phys.* **51**, 189 (1980).
33. W. A. Chupka, J. Berkowitz, *J. Chem. Phys.* **47**, 2921 (1967).
34. L. J. Frasinski *et al.*, *Phys. Rev. A* **46**, R6789 (1992).
35. R. R. Freeman *et al.*, *Phys. Rev. Lett.* **59**, 1092 (1987).
36. M. Spanner, S. Patchkovskii, *Phys. Rev. A* **80**, 063411 (2009).
37. J. Muth-Böhm, A. Becker, F. H. M. Faisal, *Phys. Rev. Lett.* **85**, 2280 (2000).
38. G. Bieri, F. Burger, E. Heilbronner, J. P. Maier, *Chim. Acta* **60**, 2213 (1977).
39. D. M. P. Holland *et al.*, *J. Phys. At. Mol. Opt. Phys.* **29**, 3091 (1996).

The Role of Driving Energy and Delocalized States for Charge Separation in Organic Semiconductors

Artem A. Bakulin,[1]* Akshay Rao,[1] Vlad G. Pavelyev,[2] Paul H. M. van Loosdrecht,[2] Maxim S. Pshenichnikov,[2] Dorota Niedzialek,[3] Jérôme Cornil,[3] David Beljonne,[3] Richard H. Friend[1]†

The electron-hole pair created via photon absorption in organic photoconversion systems must overcome the Coulomb attraction to achieve long-range charge separation. We show that this process is facilitated through the formation of excited, delocalized band states. In our experiments on organic photovoltaic cells, these states were accessed for a short time (<1 picosecond) via infrared (IR) optical excitation of electron-hole pairs bound at the heterojunction. Atomistic modeling showed that the IR photons promote bound charge pairs to delocalized band states, similar to those formed just after singlet exciton dissociation, which indicates that such states act as the gateway for charge separation. Our results suggest that charge separation in efficient organic photoconversion systems occurs through hot-state charge delocalization rather than energy-gradient–driven intermolecular hopping.

In contrast to the elegant photosynthetic apparatus evolved by nature (*1*), organic photovoltaic (OPV) cells use a single heterojunction between two semiconductors to generate charge (*2*). These semiconductors, referred to as the do-

nor (D) and acceptor (A), are cast from solution or vacuum sublimed to form a thin film with nanoscale domains of relatively pure "bulk" materials and large interfacial regions. This architecture, known as the bulk heterojunction (*3*),